Enhanced Antioxidant Ability of PEG-Coated $Ce_{0.5}Zr_{0.5}O_2$-Based Nanofluids for Scavenging Hydroxyl Radicals

Nandani Rai and S. Kanagaraj*

ABSTRACT: The antioxidant therapy to preserve residual hearing is relatively recent, and the search for effective antioxidants is still ongoing. Though nanoceria has shown promising radical-scavenging capability, improving its antioxidant ability and the dispersion stability of its nanofluid, which is critical to the desired site, i.e., cochlea, still remains a major challenge. The objective of the present work is to study the radical-scavenging capability of poly(ethylene glycol) (PEG)-coated CeO_2 and $Ce_{0.5}Zr_{0.5}O_2$ nanoparticles in water and the biologically relevant fluid (PBS buffer). Nanoparticles in the size range of 4.0−9.0 nm are synthesized using the coprecipitation method and characterized using suitable techniques. The scavenging and dispersion stability of the synthesized nanofluid are analyzed using a UV−vis spectrophotometer. It is found that the addition of PEG during the synthesis process promoted the generation of finer nanoparticles with a narrow size distribution and the doping of zirconium produced a large number of defects in the crystallite structure. The PEG coating over the nanoparticles improved the dispersion stability of nanofluids without affecting their surface reactivity, and it is found to be 94 and 80% in water and PBS, respectively, at 500 μM and 60 min, which is maintained till 90 min. The highest scavenging of hydroxyl radicals by PEG-coated $Ce_{0.5}Zr_{0.5}O_2$ is found to be 60%, which is significantly superior to that of CeO_2. The scavenging capability is found to be increased with the concentration of nanoparticles, showing the best scavenging activity at 190 and 150 μM for PEG-coated CeO_2 and $Ce_{0.5}Zr_{0.5}O_2$, respectively, and the scavenging in water is at par with that of PBS, indicating that these nanoparticles are suitable to be used in sites where a biologically relevant fluid is present, e.g., the cochlea. It is proposed that PEG-coated $Ce_{0.5}Zr_{0.5}O_2$ having an average size of ∼ 4 nm can be a potential antioxidant in relevant biomedical applications.
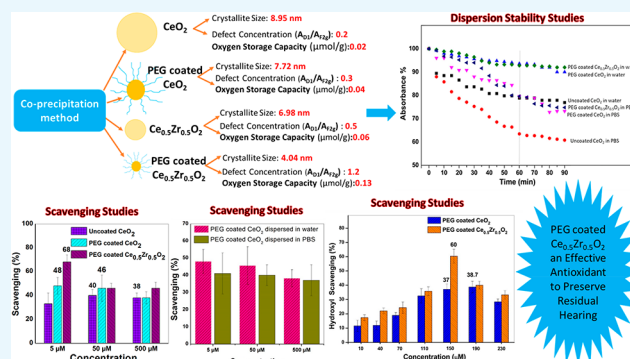
1. INTRODUCTION

The catalytic ability and regeneration characteristics of nanoceria have been tested in several reactive oxygen species (ROS)-induced disease models under both *in vitro* and *in vivo* conditions. ROS such as superoxide anions, hydrogen peroxide, and hydroxyl radicals are natural byproducts, which help during cell signalling and immune response. However, the concentration of ROS in the cell needs to be under strict regulation because of their high reactivity with the DNA and lipid membranes.[1] The effective protection by nanoceria against disease models, where the oxidative stress condition or the excess generation of ROS plays a prominent role, can be seen in several studies.[2−10] The antioxidant, antiapoptotic, anti-inflammatory, angiogenic, and antibacterial characteristics of nanoceria and its promising potential as a biomaterial for tissue engineering, wound healing, cardiac and nerve repair, and regeneration have also been reported by many researchers.[11−17] Very recently, many attempts have been focused towards assessing the protective effects of anti-inflammatory antioxidants in preserving the loss of residual hearing post cochlear implantation after evidences suggested their association with excess generation of ROS.[18−20] The first

in-human/clinical trial on minimizing the hearing loss after cochlear implant (CI) fixation used a combination of dietary antioxidants containing vitamin A, vitamin C, vitamin E, and magnesium.[21] The administration of the drug (6 tablets per day) was done orally for 105 days, which was found to preserve the hearing for 3 months after the implantation and last for a minimum of 13 years. However, the antioxidant therapy is relatively recent, whereby the protection has been achieved only to a certain extent. The search for new antioxidants with the intention of an effective outcome has become a hot topic and is currently being investigated by several research groups across the world.[22]

The protective effects of nanoceria as an antioxidant have been found to work within a range of concentrations only (0.5

$\mu g/g$,[23] 1 $\mu g/mL$,[24] 0.5 and 0.7 mg/kg,[25] and 100 $\mu g/mL$[26]), and no scavenging has been observed beyond these concentrations. Thus, the uniformity in the concentration is required to be maintained when delivering the nanoceria at the site to ensure its scavenging effects. Several attempts have been made to improve the dispersion stability of ceria nanofluids by functionalizing the nanoparticles with polymers such as dextran, poly(ethylene glycol) (PEG), chitosan, glucose, poly(vinyl alcohol) (PVA), poly(lactic-co-glycolic acid), and poly(acrylic acid).[27−29] However, maintaining the stability of the nanofluids at a pH relevant to the biological fluid has been difficult and the research is still ongoing. Glucose and dextran have been found to be susceptible to oxidation, and chitosan has been found to hinder the surface activity at higher concentrations and faces agglomeration issues at lower concentrations.[28,30] Hanafy et al.[31] have reported an improved stability of aqueous solutions of nanoceria by coating them with ethylene glycol and ethylene glycol acetate, which results from the steric hindrance effect of the polymers. Perez et al.[32] have patented the synthesis method of biodegradable polymer-coated ceria nanoparticles that are able to form a stable colloidal suspension in both water and PBS under physiological conditions (pH 7).

In order to optimize the concentration of nanoparticles for effective scavenging capability, understanding the redox activity of nanoceria is important. From the reaction mechanism of Ce^{3+} to Ce^{4+}, it is inferred that the factors that alter the Ce^{3+}/Ce^{4+} ratio, such as particle size, lattice defects, and chemical nonstoichiometry, play a pivotal role in determining the redox and catalytic properties of nanoceria.[22,33,34] In addition, the rate of regeneration of Ce^{3+} ions from Ce^{4+}, which is responsible for the long-term scavenging, is equally important as the conversion is energetically not favorable in the autoconversion process. Doping of zirconium into the ceria lattice has been found to cause structural distortions due to the difference in the ionic radiii of Ce^{4+} (0.097 nm) and Zr^{4+} (0.084 nm) and thus, the ratio of Ce^{3+}/Ce^{4+} and the catalytic activity can be tailored as per the requirement. However, the enhanced catalytic characteristics of zirconium-doped nanoceria have been so far applied in the field of manufacturing and industrial applications only.[35−43] The first study on the use of ceria-zirconia nanoparticles in controlling ROS and inflammatory diseases was reported by Soh et al.[44] They have shown that $Ce_{0.7}Zr_{0.3}O_2$ manifests significant protection against superoxide and hydroxyl radicals and successfully subsides the cycle of the inflammatory response due to the high ratio of Ce^{3+}/Ce^{4+}, which is reported to be 53%. Some of the researchers from the same group[45] have also patented the synthesis process of ceria-zirconia nanoparticles with and without a phospholipid-poly(ethylene glycol) layer and studied the scavenging ability. The zirconium doping into ceria results in increased concentration of Ce^{3+} and promotes faster reproduction of Ce^{3+} from Ce^{4+}. However, the replacement of Ce^{4+} by Zr^{4+} should be limited in such a way that it does not affect the Ce^{3+}/Ce^{4+} ratio significantly, as the ratio determines the rate of conversion between these two oxidation states. Tsai et al.[46] have reported a fourfold increase in the scavenging activity of the hydrogen peroxide radical by $Ce_{0.7}Zr_{0.3}O_2$ compared to CeO_2, and the calculations are made using catalytic reactions at high temperature with the assumption that a similar process happens at room temperature as well.

It has been shown that the presence of biologically significant anions such as sulfates, carbonates, and chloride

has no impact on the catalytic ability of nanoceria.[47] However, the exposure of ceria nanofluid to phosphate buffer at the concentration of 50 mM or more results in the formation of cerium phosphate and a corresponding loss of superoxide dismutase activity in the scavenging.[48] Though these studies reported the behavior of uncoated and undoped ceria nanofluid under biologically relevant conditions, no research details are available about the same when a coating is present and the nanoparticles are doped with zirconium.

The objective of this paper is to improve the radical-scavenging capability of CeO_2 nanoparticles by doping of zirconium and to achieve a stable nanofluid, which is critical to many biological applications, by coating the nanoparticles with PEG during the synthesis process. In order to confirm the same, the responses of PEG-coated CeO_2 and $Ce_{0.5}Zr_{0.5}O_2$ nanoparticles in two types of free radical systems, i.e., hydroxyl and DPPH radicals, has been studied and their scavenging abilities have been reported. Additionally, phosphate buffer has been used to study the effect of the presence of different ionic concentrations on the stability and scavenging capability of the nanoparticles.

2. MATERIALS AND METHODS

Cerium(III) nitrate hexahydrate $Ce(NO_3)_2 \cdot 6H_2O$, zirconyl nitrate $ZrO(NO_3)_2 \cdot xH_2O$, ammonium hydroxide 30% (NH_4OH), and PEG 600 were purchased from Loba Chemie, Mumbai, India. Hydrogen peroxide 30% and iron (II) sulfate heptahydrate were purchased from Merck Specialities Pvt. Ltd., Mumbai, India. All of the chemicals were of analytical grade and used as received without further purification.

2.1. Synthesis of Nanoparticles. PEG-coated CeO_2 and $Ce_{0.5}Zr_{0.5}O_2$ nanoparticles are synthesized using the coprecipitation method as suggested by Arya et al.[49] The selection of poly(ethylene glycol) (PEG) is done as it is an FDA-approved excipient in a variety of drug formulations owing to its water solubility, hydrophilicity, biocompatibility, and having very less side effects even at a daily dose of up to 10 mg/kg body weight.[50] PEG has also been found to be stable in the presence of strong oxidizers such as H_2O_2, which further adds to its suitability for choosing.[51,52] The selection of $Ce_{0.5}Zr_{0.5}O_2$ nanoparticles is based on our earlier studies, where different compositions of ceria-zirconia oxides ($Ce_xZr_{1-x}O_2$, where $x = 1, 0.8, 0.7, 0.6, 0.5,$ and 0.4) were assessed, and it was observed that the $Ce_{0.5}Zr_{0.5}O_2$ nanoparticles have the highest Ce^{3+} concentration and oxygen storage capacity (Synthesis and characterization of zirconia doped ceria nanoparticles as antioxidant for effective reactive oxygen species scavenging: Communicated). The synthesis method used to prepare PEG-coated CeO_2 and $Ce_{0.5}Zr_{0.5}O_2$ nanoparticles is schematically represented in Figure S1 in Supporting Information. A 0.025 M aqueous solution of cerium (III) nitrate hexahydrate ($Ce(NO_3)_2 \cdot 6H_2O$) is added in a 1 wt %/vol aqueous solution of PEG having the molecular wt of 600 g·mol^{-1} under continuous stirring. In the case of $Ce_{0.5}Zr_{0.5}O_2$, a mixed solution of zirconyl nitrate $ZrO(NO_3)_2 \cdot xH_2O$ and $Ce(NO_3)_2 \cdot 6H_2O$, each of 0.025 M, is used. To start the precipitation, the pH value of the solution is increased by adding ammonium hydroxide (2 M) at a rate of 0.1 mL/min using a microfluidic pump, and it leads to the colloidal solution. In order to obtain complete hydrolysis of the salts, the solution is stirred continuously for another 4 h. The precipitates are then washed with acetone and water, thrice each, to remove the water-soluble impurities. The centrifuged precipitates are vacuum

dried, and the obtained nanoparticles are used for further characterization and testing. For control studies, uncoated ceria nanoparticles are prepared in a similar way without adding the PEG solution and calcined at 350 °C.

2.2. Preparation of Nanofluid. The nanofluid of CeO_2 and $Ce_{0.5}Zr_{0.5}O_2$ nanoparticles with and without PEG coating is prepared via a two-step method[53] by dispersing the required amount of nanoparticles in water or PBS. A 20 min magnetic stirring and a 15 min tip sonication are employed to achieve uniform dispersion with good stability. The selection of the mixing parameter is based on the best dispersion obtained from the trial-and-error method.

2.3. Characterization. *2.3.1. Structural Characterization.* The structural characterization of all of the nanoparticles is studied using a Rigaku advanced powder diffractometer with a monochromated Cu Kα radiation (λ = 1.5406 Å) at an operating voltage of 40 kV and 112 mA current. All of the samples are scanned from 20 to 80° with a step size and speed of 0.02 and 20° per min, respectively. The phase identification is done using PDXL software and compared with the standard respective ICDD files. The average crystallite size of the nanoparticles is calculated using Scherrer's equation, where the shape factor (Scherrer constant) and wavelength of the incident X-rays are 0.94 and 1.5406 nm, respectively.

2.3.2. Morphological Characterization and Elemental Analysis. Scanning electron microscopy is performed using a Sigma 300 field emission scanning electron microscope, Ziess, fitted with in-lens SE, SE (secondary electron), and BS (backscatter electron) detectors. The samples are loaded on a carbon tape, and the data are analyzed using SmartSEM software. High-resolution transmission electron microscopy (HRTEM) images are recorded using JEOL and JEM 2100 to confirm the size, morphology and crystallinity of the nanoparticles, and energy-dispersive X-ray spectroscopy (EDX) mapping is done to assess the composition of the samples. The samples are prepared using the drop cast method on a copper-coated carbon grid and dried in an oven at 60 °C.

2.3.3. Coating Characterization. The interaction between the PEG and nanoparticles is studied using a PerkinElmer Fourier transform infrared (FTIR) spectrometer, Spectrum Two. An appropriate quantity of the sample, which is dried at 60 °C for 2 h, is mixed with dried potassium bromide (KBr) and pre-compacted at 5 MPa. An initial scan without a sample is done to detect any background noise. Samples are then scanned from 400 to 4000 cm^{-1}. The baseline correction is done as suggested by the accompanying software, Spectrum, from PerkinElmer. The transmitted rays show different types of molecular bonding based on their vibrations, rotations, or stretching.

The adsorption of the PEG coating over the nanoparticles is quantified by thermogravimetric analyzer (TGA) studies using PerkinElmer STA 8000. A weight loss between 200 and 700 °C is used to confirm the amount of PEG over the nanoparticles. The test is performed under an argon environment, which is maintained at a flow rate of 20 mL/min between 30 and 800 °C, with a heating rate of 5 °C/min as suggested by Caputo et al.[54]

The stability of the PEG coating over the nanoparticles is measured using a rheometer (Anton Paar, Physica MCR 101) by subjecting the nanofluid to a shear stress of 3 Pa at a body temperature of 37 °C and recording the change in viscosity of the nanofluids.

2.3.4. Defect Characterization. As the Raman spectroscopy can identify the configurations at the oxygen sublattice level, Raman studies are performed to confirm the presence of oxygen vacancies in the lattice. Raman spectra are recorded at room temperature using a Laser Micro RAMAN spectroscope (Jovin Yvon, triax 550) equipped with a CCD detector. A monochromatic light of 488 nm is used as the source of excitation.

The oxygen storage capacity (OSC) of the nanoparticles is evaluated by the thermogravimetry technique (PerkinElmer STA 8000) as suggested by Ozawa et al.[55] in the temperature range of 300−800 °C to assess the concentration of oxygen vacancies. The samples are (1) heated from 30 to 800 °C under argon, (2) cooled down to 150 °C in air, and (3) heated again from 150 to 800 °C in air at a heating/cooling rate of 10 °C/min. The weight loss of the nanoparticles during the second heating cycle corresponds to the oxygen release capacity of the nanoparticles, which is then converted to the oxygen vacancy content or OSC using the involved reactions.

2.3.5. Effect of PEG Coating on the Stability of the Nanofluid. The stability of the nanofluid is quantitatively evaluated using a UV−vis spectrophotometer, model UVmini 1240. The UV absorbance at 300 nm is obtained at different intervals for 1 h, and the change in percentage of absorbance is calculated using eq 1.

$$\text{absorbance } \% = \frac{A_t}{A_0} \times 100 \tag{1}$$

where A_t and A_0 are the absorbance at time t and absorbance at time $t = 0$, respectively.

2.3.6. Radical Scavenging Study. The free radical-scavenging capability of the nanoparticles is studied using DPPH (2,2-diphenyl-1-picrylhydrazyl) assay. DPPH (100 μL of 0.1 mM) is added to the nanoceria solutions with different concentrations (0, 5, 50, and 500 μM), and the absorbance is measured at 517 nm after 30 min of incubation in the dark. The radical scavenging is calculated in terms of percentage inhibition or quenching using a commonly used expression (eq 2),[56] where A_t and A_0 are the absorbance of the DPPH solution with and without the antioxidant, respectively.

$$I\% = \frac{A_0 - A_t}{A_0} \times 100 \tag{2}$$

2.3.7. Hydroxyl Scavenging Study. Methyl violet (MV) at a concentration of 50 μM is used as an indicator. Dispersed solutions of nanoceria are prepared in a similar way as in the case of the dispersion stability tests. The prepared test solutions are as follows: (1) water + MV; (2) water + MV + $FeSO_4$ + H_2O_2; and (3) water + MV + $FeSO_4$ + ceria/ceria-zirconia nanoparticles + H_2O_2. The test solution of 4 mL is added in the same order as mentioned above, and the absorbance is recorded after 5 min of the incubation period. In order to ensure that the reaction solutions do not have any effect on the absorption of MV, the absorption spectrum of each reaction solution with the base solution (water + MV) is also measured and compared.

3. RESULTS AND DISCUSSION

3.1. Structural Analysis by X-ray Diffraction (XRD). XRD was performed to measure the solid solubility, crystallite size, and lattice parameters of the nanoparticles. The XRD patterns of all of the test samples along with their

corresponding standard ICDD files 00-004-0593 (CeO$_2$), 00-007-0343 (ZrO$_2$), and 01-076-8752 (Ce$_{0.5}$Zr$_{0.5}$O$_2$) are shown in Figure 1. The four strongest peaks of CeO$_2$ nanoparticles
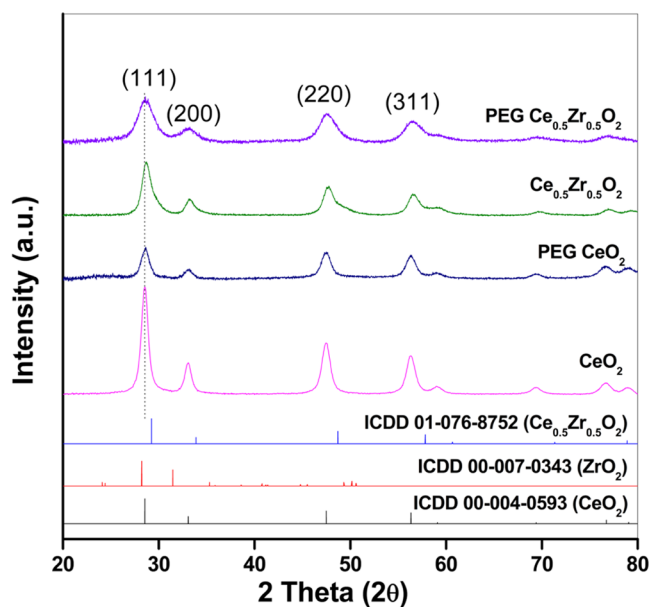

Figure 1. XRD patterns of nanoparticles.

without PEG coating appear at around 28.5, 33.0, 47.4, and 56.2°, corresponding to the respective (111), (200), (220), and (311) crystallographic planes of the cubic fluorite structure. There is a positive shift of peaks by 0.1° for PEG-coated CeO$_2$ at smaller 2θ (28.5, 33.0°) angles. The XRD spectra of Ce$_{0.5}$Zr$_{0.5}$O$_2$ nanoparticles without PEG coating showed four major peaks at around 28.6, 33.3, 47.7, and 56.5° assigned to the cubic fluorite structure of Ce$_{0.5}$Zr$_{0.5}$O$_2$. The negative shift in the peak position is observed in the PEG-coated Ce$_{0.5}$Zr$_{0.5}$O$_2$, which varies in the range of 0.2−0.3° at smaller 2θ (28.6, 33.3°) angles and in the range of 0.5−0.6° at higher 2θ (47.7 and 56.5°) angles. The peak positions are directly related to the interplanar spacing (d) by Bragg's law. As the experimental conditions have been kept the same for all of the samples, it is assumed that the shift does not arise from the instrumental causes and is due to the variation of the interplanar spacing of the samples. The peaks corresponding to the separate phase of ZrO$_2$ are not found, which indicates that a homogeneous solid solution of Ce$_{0.5}$Zr$_{0.5}$O$_2$ is formed.

It is also observed from Figure 1 that the order of peak broadening is as follows: CeO$_2$ < PEG-coated CeO$_2$ < Ce$_{0.5}$Zr$_{0.5}$O$_2$ < PEG-coated Ce$_{0.5}$Zr$_{0.5}$O$_2$. This implies that the size of the nanoparticles gets reduced by the addition of PEG during the synthesis process and the doping of zirconium into the ceria lattice. The average crystallite size obtained from Scherrer analysis on the peaks (111) and (220) and the lattice parameters of the nanoparticles are summarized in Table 1.

It is observed that under similar synthesis conditions, zirconium-doped samples showed smaller crystallite sizes, 4.04 and 6.98 nm for Ce$_{0.5}$Zr$_{0.5}$O$_2$ with and without PEG coating, respectively, compared to the undoped nanoparticles, 7.72 and 8.95 nm for CeO$_2$ with and without PEG coating, respectively. Controlling the size of the ceria nanoparticles is critical to the antioxidant ability, and it has been found that by doping with transition and nontransition metal ions (Al^{3+}, Si^{4+}, Ti^{4+}, Zr^{4+}, etc.) the size can be reduced, keeping the synthesis conditions

Table 1. Influence of the Synthesis Method and Doping of Zirconium in Ceria

	2θ for highest intensity (deg)	crystallite size (nm)	lattice parameter (Å)
CeO$_2$	28.5	8.95	5.41
PEG-coated CeO$_2$	28.6	7.72	5.40
Ce$_{0.5}$Zr$_{0.5}$O$_2$	28.6	6.98	5.39
PEG-coated Ce$_{0.5}$Zr$_{0.5}$O$_2$	28.5	4.04	5.43

similar.[35] The smaller crystallite size of ceria-zirconia catalysts compared to ceria is due to the relaxation of the strain induced by the substitution of Ce^{4+} ions (0.97 Å) by smaller Zr^{4+} ions (0.84 Å) and has been reported in many studies.[36,57] The smaller size of PEG-coated nanoparticles is due to the fact that the coordination between PEG and the cerium ion affects the hydrolysis reaction as shown in Figure 2, which influences the frequency of nucleation and growth. The hydrolysis reaction is the primary stage of formation of the cerium oxide nucleus. When the cerium salt is dissolved in water, there is a partial charge transfer from the water molecule to the empty "d" orbitals of the cerium cation. Depending on the magnitude of the charge transfer and synthesis conditions, a large number of possible precursors may form from the following auqo-hydroxo and hydroxo complexes (Figure 2).[59]

The oxygen molecules of the ether group and the terminal OH group of the PEG act as a base and help in hydrolysis and the nucleation process. After the formation of cerium oxide nanocrystals, the molecules of PEG coat over them, restricting their further growth. The smaller size of ceria nanoparticles in the presence of the polymer during the synthesis process has also been reported in several studies.[27,52,60,61]

It is observed from Table 1 that the lattice parameters do not differ much in the case of CeO$_2$ and PEG-coated CeO$_2$ despite their being a significant difference in their respective crystallite sizes. The lattice parameter of Ce$_{0.5}$Zr$_{0.5}$O$_2$ is found to contract compared to that of the pure ceria. The decrease of lattice size upon the addition of zirconium into the ceria lattice is due to the smaller ionic radius of Zr^{4+} (0.84 Å) compared to Ce^{4+} (0.97 Å). The same kind of observation was also reported by Chen et al.[62] and Deng et al.[63] However, the lattice parameter of PEG-coated Ce$_{0.5}$Zr$_{0.5}$O$_2$ is found to be increased in comparison to that of pure ceria. The increased lattice parameter despite having a smaller ionic radius of zirconium in the lattice suggests the generation of more number of Ce^{3+}. The ionic radius of Ce^{3+} is 1.03 Å, which is larger than that of Ce^{4+} (0.97 Å) or Zr^{4+} (0.84 Å). Due to the generation of more number of Ce^{3+} having a higher ionic radius, it is found to dominate over the doping effect from the zirconium having a lower ionic radius, resulting in lattice expansion and an increased lattice parameter. The above proposed hypothesis is also supported by the study carried out by Deshpande et al.,[64] who established a correlation between the particle size and the lattice parameter in nanoceria in the size range of 3−30 nm and found an increasing trend of the lattice size with the reduction of the size of nanoparticles, which is also observed in our study.

3.2. Morphological Characterization and Elemental Analysis. The morphology and uniformity of the synthesized nanoparticles have been studied using SEM and TEM. Figure 3a−d presents the TEM images of the CeO$_2$ and Ce$_{0.5}$Zr$_{0.5}$O$_2$ nanoparticles with and without PEG coating. The SEM images of the samples are given in Figure S2a−d of the supplementary

$$Ce^{4+} + : O\begin{matrix} H \\ \\ H \end{matrix} \rightleftharpoons \left[Ce \leftarrow O\begin{matrix} H \\ \\ H \end{matrix} \right]^{4+} + H^+ \rightleftharpoons \left[Ce \leftarrow O - H \right]^{3+} + 2H^+$$

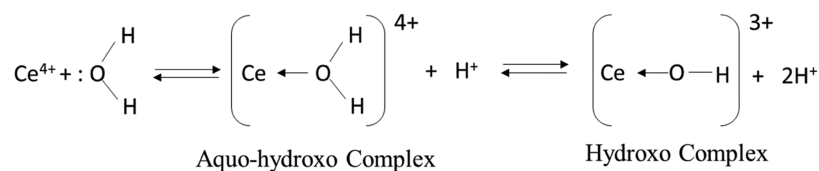Aquo-hydroxo Complex   Hydroxo Complex

Figure 2. Hydrolysis of cerium cation and formation of possible precursors.
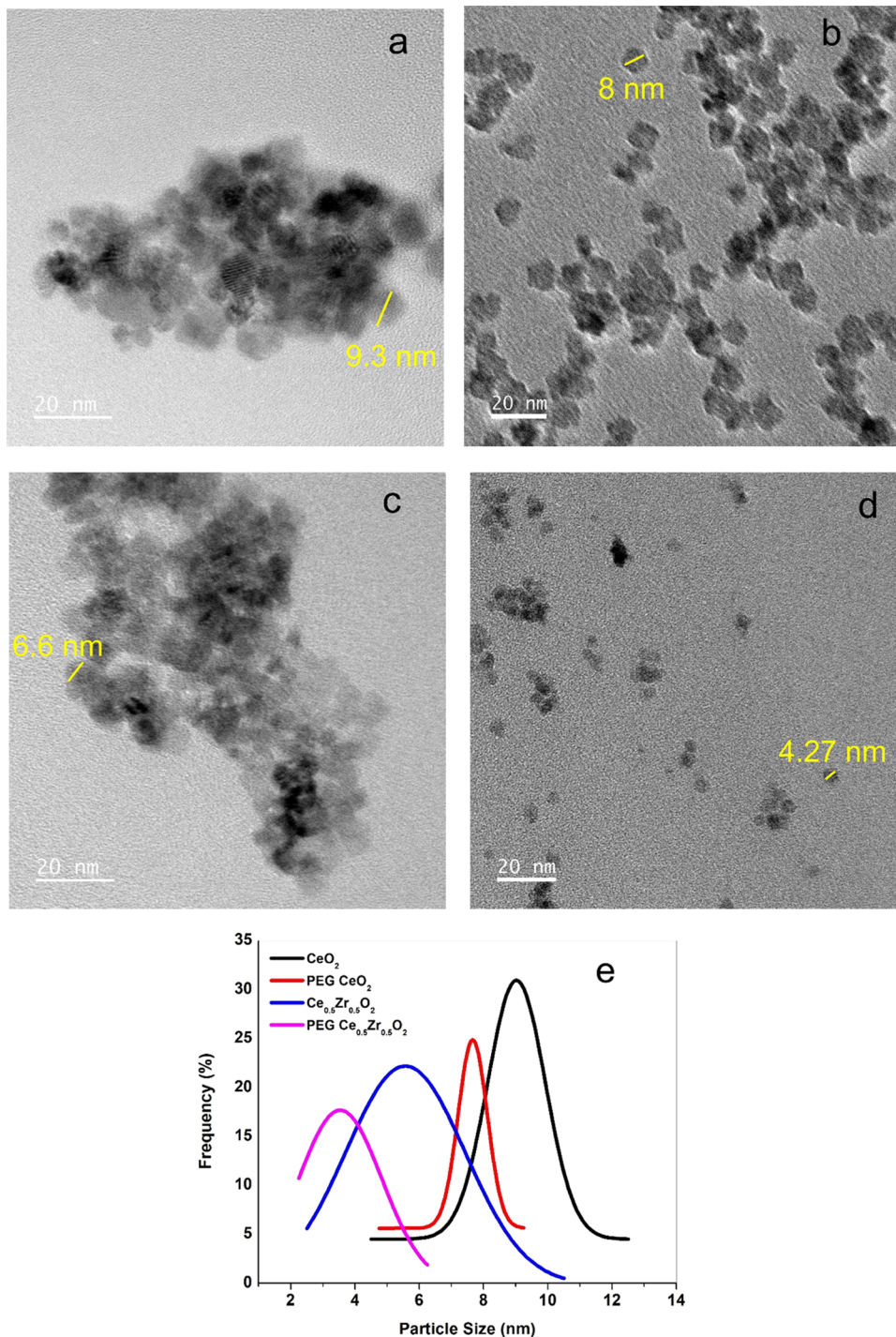
Figure 3. TEM images of the nanoparticles and the comparative particle size distribution. (a) CeO_2; (b) PEG-coated CeO_2; (c) $Ce_{0.5}Zr_{0.5}O_2$; (d) PEG-coated $Ce_{0.5}Zr_{0.5}O_2$; and (e) comparative particle size distribution.

document. The precipitation method followed in this study yielded spherical nanoparticles. It is known that nanoparticles with sharp edges cause mechanical damage to the cell membranes and therefore, are considered to be less
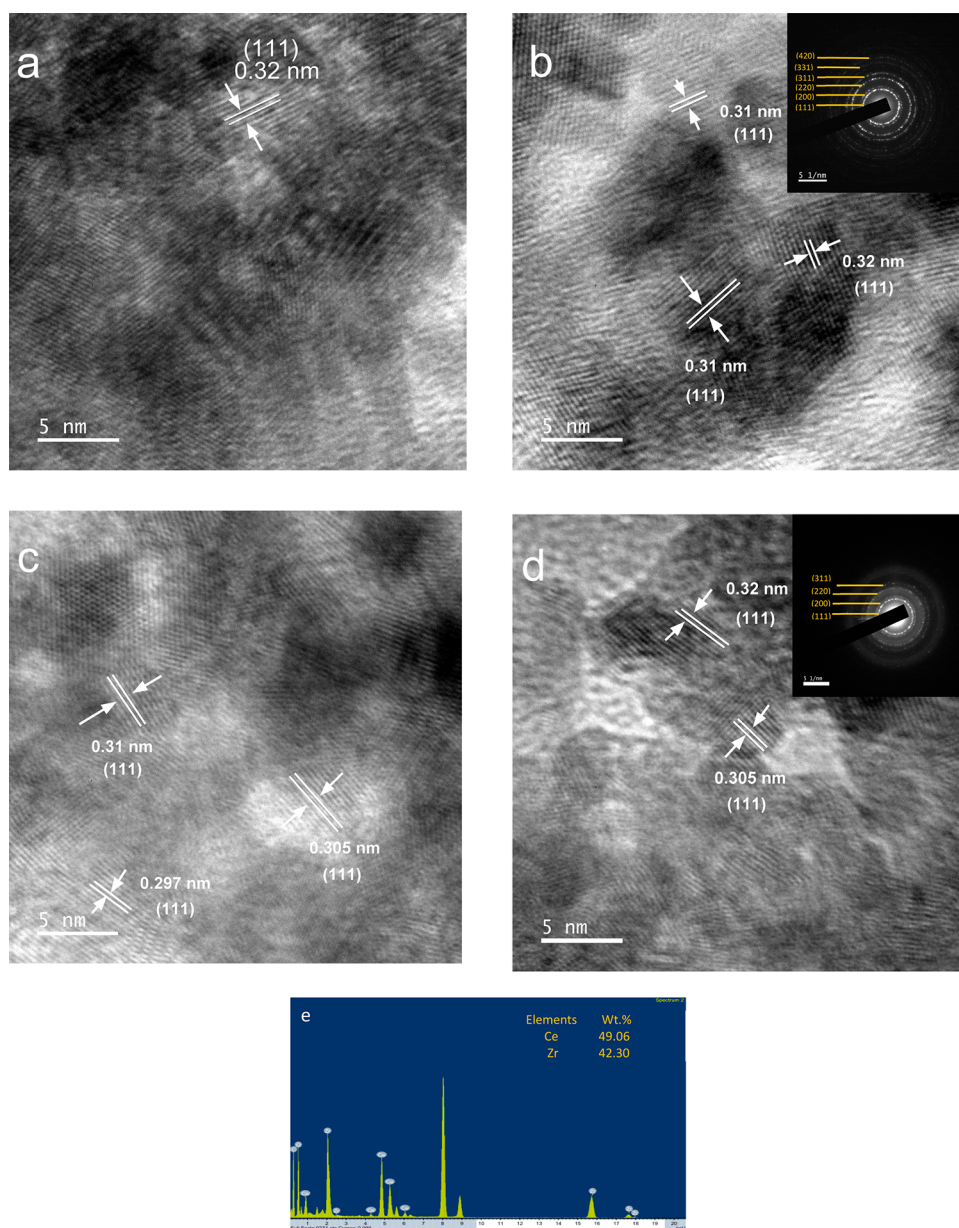
Figure 4. HRTEM images and EDX of the nanoparticles. (a) CeO_2; (b) PEG-coated CeO_2; (c) $Ce_{0.5}Zr_{0.5}O_2$; (d) PEG-coated $Ce_{0.5}Zr_{0.5}O_2$; and (e) EDX spectra of PEG-coated $Ce_{0.5}Zr_{0.5}O_2$.

biocompatible.[65] The spherical shape of the nanoparticles obtained in our study eliminates such occurrences. In addition, the size of the spherical nanoparticles is found to influence the scavenging of different types of radicals significantly at the desired biological site, i.e., cochlea.[58] The size distribution of the nanoparticles is measured using ImageJ software from the TEM images and is shown in Figure 3e. The average particle sizes of the samples were calculated to be 9.03 ± 1, 7.67 ± 1, 5.89 ± 1, and 3.75 ± 1 nm for CeO_2, PEG-coated CeO_2, $Ce_{0.5}Zr_{0.5}O_2$, and PEG-coated $Ce_{0.5}Zr_{0.5}O_2$, respectively, which is in good agreement with the results obtained from the SEM (Figure S3) and XRD studies. The presence of PEG during the synthesis process resulted in finer and uniformly sized nanoparticles with a narrow size distribution. The better control over the morphological characteristics is believed to be due to the uniform growth process caused by the coating of PEG over the nanoparticles, and it is also supported by Djuričić et al.[66] The appearance of the PEG-coated samples is

in the form of short chain-like clusters, which is consistent with the studies by Karakoti et al.[30] The HRTEM images (Figure 4a−d) showed that all of the samples exhibited the (111) plane as the preferred plane ($d = 0.31 \pm 2\%$ nm) on the surface. The SAED pattern shown in the inset (Figure 4b,d) shows the diffraction rings corresponding to the (111), (200), (211), and (311) planes, which confirmed the polycrystalline nature and cubic fluorite structure of the nanoparticles. TEM EDX analysis of PEG-coated $Ce_{0.5}Zr_{0.5}O_2$ (Figure 4e) showed that Ce and Zr were present in a ratio of close to 1:1, confirming that the synthesized $Ce_{0.5}Zr_{0.5}O_2$ has an almost stoichiometric composition. The elemental mapping of PEG-coated $Ce_{0.5}Zr_{0.5}O_2$ shown in Figure S4 of the supplementary document confirmed the uniform distribution of Ce and Zr in the sample and the formation of a homogeneous solid solution.

3.3. Coating Characterization. The interaction between the ceria nanoparticles and PEG is confirmed by FTIR studies,

and the spectra obtained from the studies are shown in Figure 5. The IR spectra of PEG showed the transmission bands at
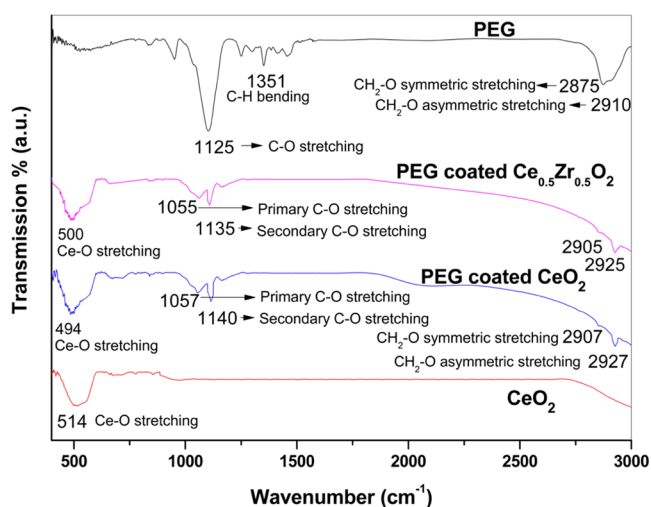

Figure 5. FTIR spectra of PEG, PEG-coated nanoparticles, and uncoated ceria nanoparticles.

1125, 1351, 2875, and 2910 cm^{-1} generated due to the characteristic C-O stretching mode, C-H bending vibrations, CH$_2$-O symmetric, and CH$_2$-O asymmetric stretching vibrations, respectively.[67] Both PEG-coated CeO$_2$ and Ce$_{0.5}$Zr$_{0.5}$O$_2$ exhibited a sharp peak at around 2927 cm^{-1} and a relatively low intensity peak at around 2905 cm^{-1}, corresponding to the characteristic asymmetric and symmetric stretching of CH$_2$-O bonds. The peaks observed at 1057 and 1140 cm^{-1} in PEG-coated CeO$_2$ and at 1055 and 1135 cm^{-1} in PEG-coated Ce$_{0.5}$Zr$_{0.5}$O$_2$ occur due to the primary and secondary C-O stretching vibrations, respectively.[67] The shift in the peak position from 1125 cm^{-1} as seen in the PEG samples to 1140 and 1135 cm^{-1} in the case of PEG-coated CeO$_2$ and Ce$_{0.5}$Zr$_{0.5}$O$_2$, respectively, resulted from the change in the surrounding electric field.[63] The broad band observed at around 514, 494, and 500 cm^{-1} in CeO$_2$, PEG-coated CeO$_2$, and Ce$_{0.5}$Zr$_{0.5}$O$_2$, respectively, is the characteristic peak of CeO$_2$.[68] The presence of characteristic peaks of C-O and CH$_2$-O stretching in the PEG-coated samples confirmed the formation of PEG coating, and it was also reported by Karakoti et al.[69]

To further confirm the coordination between PEG and nanoparticles, thermogravimetry analysis (TGA) is done. The weight loss against the temperature of all of the samples along with PEG has been shown in Figure 6, which reveals two main regions of weight loss of the nanoparticles. The first weight loss of about 3, 6, 23, and 25% occurs for CeO$_2$, Ce$_{0.5}$Zr$_{0.5}$O$_2$, PEG-coated CeO$_2$, and PEG-coated Ce$_{0.5}$Zr$_{0.5}$O$_2$, respectively, at <200°C, which is associated with the loss of adsorbed water. The uncoated samples of CeO$_2$ and Ce$_{0.5}$Zr$_{0.5}$O$_2$ did not show any secondary weight loss in the temperature range of 200–700 °C. However, the PEG-coated CeO$_2$ and Ce$_{0.5}$Zr$_{0.5}$O$_2$ samples showed 3% secondary weight loss between 200 and 700 °C, which is attributed to the decomposition of the PEG coating present on the surface of the nanoparticles. The amount of secondary weight loss between 200 and 700 °C is in agreement with the coordination of PEG as an adsorbed layer over the nanoparticles.[54]

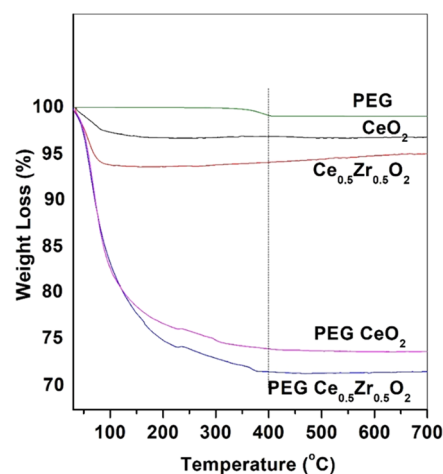**Figure 6.** Weight loss percentage of the nanoparticles in the temperature range of 35−700 °C under argon environment.

The stability of the PEG coating is studied by subjecting the nanofluids of all of the nanoparticles synthesized in water to shear stresses of up to 3 Pa and recording the change in the viscosity at a body temperature of 37 °C. The maximum shear stress that a cochlea can withstand has been reported to be around 1.5 Pa.[70] The concentration of the nanofluid used in the study is 200 μM, which was selected from the results of scavenging studies. The results are shown in the Figure S5 of the Supporting Information. No change in the viscosity of the nanofluids of PEG-coated and corresponding uncoated nanoparticles has been found up to 3 Pa of shear stress. This result suggests that the PEG coating is stable and can stay over the nanoparticles even after long-term usage.

3.4. Defect Characterization. *3.4.1. RAMAN Spectroscopy.* The Raman spectra of the nanoparticles in the range of 200−800 and 500−650 cm^{-1} are shown in Figure 7a,b, respectively. The peak positions and the area under the peak are examined by fitting the data to the Lorentz line shape.

All of the samples showed a strong peak in the range of 460−465 cm^{-1}, which corresponds to the Raman active F$_{2g}$ vibration mode, confirming the presence of a cubic fluorite structure. The position of the F$_{2g}$ band corresponding to the symmetrical stretching of Ce-O8 units occurs at 465 cm^{-1}, which is characteristic of fully oxidized CeO$_2$. It is also observed that the F$_{2g}$ band shifts to 460 and 458 cm^{-1}, respectively, in the case of uncoated CeO$_2$ and PEG-coated nanoparticles. The shift in the frequency of Raman mode occurs due to the variation of the lattice size. The expansion of the lattice size in uncoated and PEG-coated CeO$_2$ occurs when the ceria reduces from Ce^{4+} to Ce^{3+} state, accompanied by the formation of oxygen vacancies. This happens due to the presence of unbalanced attractive forces between the vacancy of the neighboring Ce^{4+} cation and the oxygen anion opposite to the vacancy site, leading to the outward relaxation of the Ce^{4+} cation,[71] and as a consequence, a peak shift towards lower frequency is observed. The incorporation of zirconium into the ceria lattice leads to a blue shift from 460 to 464 cm^{-1} in the case of uncoated Ce$_{0.5}$Zr$_{0.5}$O$_2$ and from 458 to 464 cm^{-1} in the case of PEG-coated Ce$_{0.5}$Zr$_{0.5}$O$_2$. The position and width of the peaks are characteristics that are sensitive to the defects induced in the oxygen ion sublattice. As the size of the zirconium ion, Zr^{4+} (0.84 Å), differs from Ce^{4+} (0.97 Å), the introduction of zirconium into the ceria lattice induces change
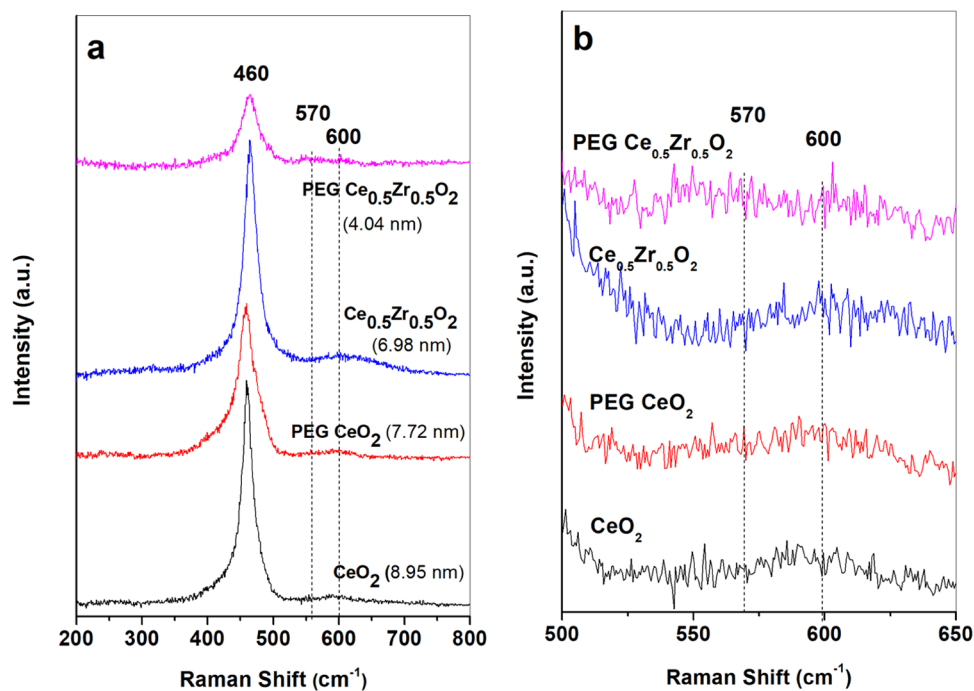
Figure 7. Raman spectra of CeO_2 and $Ce_{0.5}Zr_{0.5}O_2$ nanoparticles with and without PEG coating in the range (a) 200−800 cm^{-1} and (b) 500−650 cm^{-1}.

in the crystal lattice and affects the surroundings of the metal cations around the oxygen ion. As a consequence, the blue shift of the peaks is observed and it is in good agreement with other published articles.[72,73] The appearance of additional modes other than F_{2g} occurs due to the reduction of ceria from Ce^{4+} to Ce^{3+} state, formation of oxygen vacancies, and the association of the Zr^{4+} with the vacancies. In the case of CeO_2 and PEG-coated CeO_2 samples, the peaks appear near 270, 553, and 590 cm^{-1} and in the case of $Ce_{0.5}Zr_{0.5}O_2$ and PEG-coated $Ce_{0.5}Zr_{0.5}O_2$ samples, the peaks appear near 320, 570, and 600 cm^{-1}, which are attributed to the presence of defect-related Raman modes though their source of origin is still controversial.[71] The peaks appeared at around 554 and 591 cm^{-1}, 552 and 590 cm^{-1}, 573 and 600 cm^{-1}, and 567 and 602 cm^{-1} for CeO_2, PEG-coated CeO_2, $Ce_{0.5}Zr_{0.5}O_2$, and PEG-coated $Ce_{0.5}Zr_{0.5}O_2$, respectively, corresponding to the oxygen defects and are denoted as the "D" band. As per the latest studies,[72] one of the two components of the "D" band, D1 (at about 560 cm^{-1}), has been assigned to the stretching vibration of Ce^{3+}--O--Ce^{4+} due to the presence of oxygen defects, and D2 (at about 600 cm^{-1}) has been assigned to the stretching vibration of Zr^{4+}--O--Ce^{4+} bonds without oxygen defects in doped ceria nanoparticles.

The concentrations of the oxygen defects have been quantitatively measured by the ratio of the "D1" band peak area to that of F_{2g} (A_{D1}/A_{F2g}), as suggested by Xu et al.,[72] and have been summarized in Table 2. The value of the A_{D1}/A_{F2g} ratio is found to be 0.2, 0.3, 0.5, and 1.2 for CeO_2, PEG-coated CeO_2, $Ce_{0.5}Zr_{0.5}O_2$, and PEG-coated $Ce_{0.5}Zr_{0.5}O_2$, respectively. The higher value of A_{D1}/A_{F2g} in ceria-zirconia oxides indicates that the doping with zirconium into ceria causes more generation of defects. During the synthesis process, the distance between the zirconium cation and oxygen anion (Zr-O) bonds is responsible for the lower energy for oxygen removal and ease of defect formation.[74] The replacement of the Ce^{4+} cation by a Zr^{4+} cation in ceria-zirconia oxides causes

Table 2. Influence of the Synthesis Method and Introduction of Zirconium on the Defect Concentration

	CeO_2	PEG CeO_2	$Ce_{0.5}Zr_{0.5}O_2$	PEG $Ce_{0.5}Zr_{0.5}O_2$
peak F_{2g} (cm^{-1})	460	458	465	464
peak 'D1' band (cm^{-1})	554	552	573	567
A_{D1}/A_{F2g}	0.2	0.3	0.5	1.2

geometrical changes, in which the Zr-O bond is under a tensile strain of approx. 3%[75] due to the difference in sizes of both the cations. When the oxygen vacancy forms at a site neighboring the Zr^{4+} cation, three of the Ce-O bonds and one of the Zr-O bonds break, resulting in a significant release of the energy due to the relaxation of the Zr-O bond, and thus lowering the oxygen vacancy formation energy.[75] It can be concluded from the Raman studies that zirconium doping induced more distortion in the lattice and subsequently resulted in an increased number of oxygen vacancies.

3.4.2. Oxygen Storage Capacity Measurements. The OSC is used to evaluate the catalytic activity of the metal oxides and is related directly to the concentration of oxygen vacancies present in the catalyst.[46] The room temperature scavenging ability of $Ce_xZr_{1-x}O_2$ nanoparticles has been found to correlate well with the OSC values at high temperature.[46] Figure S6 shows the weight loss percentage of the nanoparticles during the second heating cycle in the temperature range of 300−800 °C, from which the OSC values have been calculated by using the reactions involved in the process and have been listed in Table 3. The PEG-coated $Ce_{0.5}Zr_{0.5}O_2$ showed the highest OSC, indicating that the zirconium incorporation has led to an increase in the number of oxygen vacancies. The results are consistent with the RAMAN studies.

3.5. Effect of PEG Coating on the Stability of the Nanofluid. The dispersion stability of the nanofluid is tested at 500 μM, which was selected based on the highest

Table 3. Oxygen Storage Capacity (OSC) of the Nanoparticles

	OSC (δ) (μmol/g)
CeO_2	0.02
PEG-coated CeO_2	0.04
$Ce_{0.5}Zr_{0.5}O_2$	0.06
PEG-coated $Ce_{0.5}Zr_{0.5}O_2$	0.13

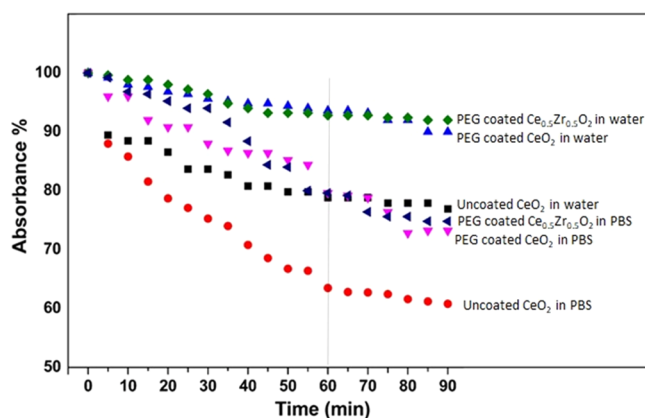concentration used in the scavenging study. Figure 8 shows the change in absorbance with time for the nanofluid of CeO_2 and

Figure 8. Absorbance/dispersion stability of the nanofluid (500 μM) in water and PBS.

$Ce_{0.5}Zr_{0.5}O_2$ nanoparticles with and without PEG coating in water and PBS buffer. The concentration of the absorbing species in the solution has a linear relationship with the absorbance as per Beer–Lambert law. Therefore, the change of absorbance with time is used as a measure of the relative stability of the nanofluids.[76]

It is observed from Figure 8 that the presence of PEG coating over the CeO_2 nanoparticles has improved their dispersion stability both in water and in PBS buffer. The dispersion stability of PEG-coated $Ce_{0.5}Zr_{0.5}O_2$ samples is at par with that of PEG-coated CeO_2 in water and PBS, and it is found to be 94 and 80%, respectively, at 60 min. Then, there is no change in absorbance, i.e., the stability of the nanofluid is maintained till 90 min. The dispersion stability of the uncoated CeO_2 is only 79 and 63% in water and PBS, respectively. To study the scavenging ability of the nanoparticles, the nanofluid is required to have a good stability up to 60 min to minimize the variation resulting from the possible sedimentation. As the PEG-coated nanofluid is found to fulfill the mentioned requirement, it has been used further in scavenging studies. On comparing the stabilities of PEG-coated CeO_2 and $Ce_{0.5}Zr_{0.5}O_2$-based nanofluids prepared in water and PBS buffer, it is observed that the stability is reduced in PBS buffer by 14% compared to water-based nanofluids. The lower stability in phosphate buffer could be attributed to the negatively charged phosphate ions binding with the positively charged nanoceria, which minimizes the effect of electrostatic repulsion between the nanoparticles. The van der Waals attraction dominates, resulting in agglomeration. The proposed hypothesis has been supported by the earlier studies.[48,77] The improved dispersion stability of the PEG-coated samples is believed to arise from the steric stabilization resulting from the adsorbed polymeric layer, which offsets the van der Waals force

that drives the agglomeration. A simple mechanism of steric stabilization by PEG has been shown in Figure 9 with the
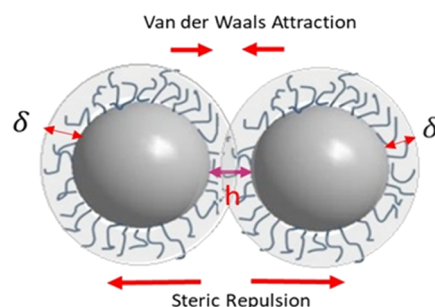

Figure 9. Schematic diagram of the energy interaction as a function of the distance between two sterically stabilized nanoparticles in the suspension.

assumption that the PEG has strong adsorption with the nanoparticles and forms a full coverage. Depending on the system, different surface forces arise when the colloidal particles approach within the range of interaction. The universal van der Waals force of attraction arises due to the fluctuations in the electron clouds surrounding the atoms and increases rapidly at short separation. In the absence of any repulsive force in the system, this results in particle aggregation followed by sedimentation. In the presence of PEG, the nanoparticles experience a repulsive force when the distance between two particles goes below twice the thickness of the polymer layer due to volume restriction and osmotic effects in the region between the two surfaces. The total interaction potential in any colloidal system is a summation of the van der Waals force of attraction and steric repulsion. The attractive van der Waals forces are particularly strong at a short distance. The presence of the PEG layer prevents the particles from approaching each other to a short distance where the highly attractive forces dominate,[78] and thus, it prevents sedimentation.

3.6. Radical Scavenging Study. The antioxidant ability has been assessed using DPPH (2,2-diphenyl-1-picrylhydrazyl) assay at 5, 50, and 500 μM concentrations and the results are shown in Figure 10a,b. It can be seen from Figure 10a that the scavenging of radicals for uncoated CeO_2, PEG-coated CeO_2, and PEG-coated $Ce_{0.5}Zr_{0.5}O_2$ ranges from 33 to 40, 38 to 46, and 46 to 68%, respectively, when a lower, an intermediate, and a higher concentration, i.e., 5, 50, and 500 μM, are used during the test. The result indicates that the presence of the coating does not hamper the surface reactivity of the nanoparticles. The performance of the PEG-coated CeO_2 nanofluid is found to be slightly improved compared to the uncoated CeO_2 at 5μM. It might be because of the excellent dispersion stability of the PEG-coated CeO_2 (94%) compared to the uncoated CeO_2 (79%), which could have led to a reduced delivery of CeO_2 nanoparticles than expected in the test solution and scavenging process. However, the difference becomes less significant with increasing concentration. As sedimentation is a dynamic phenomenon, the prediction of the exact variation of the concentration in the three test systems and the corresponding effects are uncertain. The scavenging of radicals by PEG-coated $Ce_{0.5}Zr_{0.5}O_2$ is seen to be 68%, whereas PEG-coated CeO_2 can scavenge only 48%. The improved scavenging by PEG-coated $Ce_{0.5}Zr_{0.5}O_2$ is due to the smaller size of the nanoparticles. With the reduction of the size, the
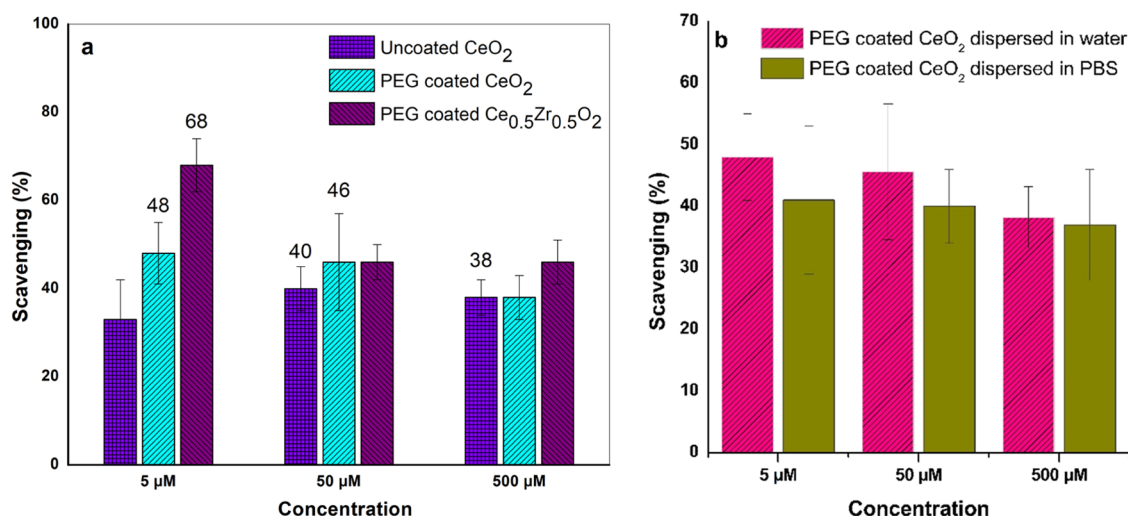
Figure 10. Radical scavenging of nanoceria-based fluids. (a) Effect of PEG coating and Zr doping; (b) effect of PBS buffer ions.

concentrations of defects and oxygen vacancies have been found to be increased, as confirmed from the RAMAN and OSC studies; $A_{D1}/A_{F2g} = 1.2$ and OSC = 0.13 for PEG-coated $Ce_{0.5}Zr_{0.5}O_2$ compared to $A_{D1}/A_{F2g} = 0.3$ and OSC = 0.04 for PEG-coated CeO_2, resulting in improved catalytic activity and radical-scavenging abilities of the nanomaterials. The effect of the smaller particle size of ceria (in the range of 3−5 nm) in controlling ROS-induced damages can be seen in many *in vitro* and *in vivo* models, which is described in the review paper.[58] The scavenging is also found to be the best at a lower concentration i.e., at 5 μM.

Figure 10b highlights the behavior of nanoceria in the presence of biologically relevant ions. The radical scavenging is found to be 7, 6, and 1% lower in PBS buffer at concentrations of 5, 50, and 500 μM, respectively, compared to water. However, the difference is not significant, and it can be concluded that the presence of ions in PBS buffer does not interfere with the scavenging ability of the nanoparticles. The result is consistent with the studies by Xue et al. where the presence of biologically significant anions such as sulfates, carbonates, and chloride has been found to have no impact on the catalytic ability of nanoceria.[47]

3.7. Hydroxyl Scavenging Study. The hydroxyl radicals are known to be the most reactive and harmful type of ROS.[79] The scavenging ability of nanoparticles is tested as suggested by Lu et al.[80] using the MV-Fenton system, where the hydroxyl radicals are generated by a Fenton system of 3.6 mM $FeSO_4$ + 1 M H_2O_2 that produces optimum hydroxyl radicals to be displayed clearly in the UV spectrophotometer. The associated reaction is given in the eq 3.

$$Fe^{2+} + H_2O_2 \rightarrow Fe^{3+} + OH^- + OH^\bullet \qquad (3)$$

The reaction between the hydroxyl free-radical and methyl violet and the corresponding change in the maximum absorbance of methyl violet are shown in Figure S7. It is seen that the aqueous solution of methyl violet shows a purple color, which produces the characteristic absorbance peak at about 582 cm^{-1} in the UV spectrophotometer. Upon exposure to the Fenton system, the solution becomes colorless because of the reaction of MV with the generated hydroxyl free-radical, and therefore, the intensity of the maximum absorbance is observed to decrease. When nanoparticles are added, due to their scavenging effect, some of the hydroxyl radicals are

expected to convert into water, and thus, the number of radicals that react with methyl violet is expected to reduce. Hence, the intensity of the maximum absorbance of methyl violet is expected to be less affected by a hydroxyl free-radical system when nanoceria is present.

The scavenging capabilities of nanoparticles in the concentration range of 10−230 μM have been studied parametrically. Percentage scavenging is calculated by measuring the change in the absorbance value of methyl violet upon the addition of hydroxyl free-radicals in presence and absence of CeO_2 and $Ce_{0.5}Zr_{0.5}O_2$ nanoparticles as suggested in ref 81 and is given in eq 4.

$$\text{percentage scavenging} = \frac{\Delta A - \Delta a}{\Delta A} \times 100 \qquad (4)$$

where ΔA and Δa are the changes in the absorbance of the methyl violet solution after the addition of OH$^\bullet$ radicals in the absence and presence of nanoparticles, respectively.[80] The results are plotted in Figure 11, where it is observed that all of the nanoparticles showed the scavenging capability at all concentrations. The scavenging exhibited by PEG-coated CeO_2 and $Ce_{0.5}Zr_{0.5}O_2$ ranges from 12−39 and 17−60%,
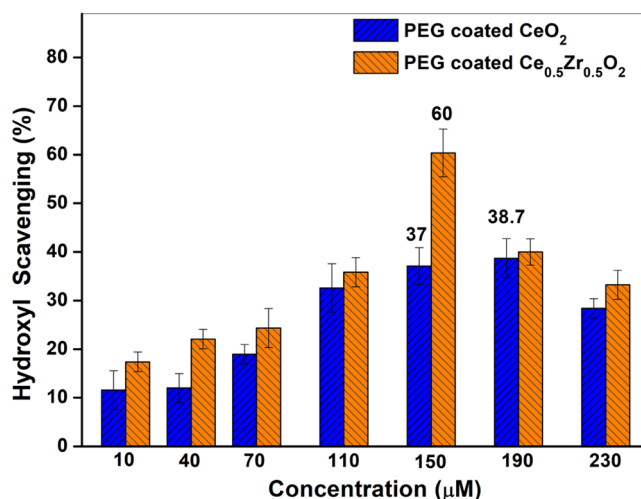

Figure 11. Hydroxyl scavenging (%) of PEG-coated nanoparticles at different concentrations.

respectively, and at each concentration, the scavenging by PEG-coated $Ce_{0.5}Zr_{0.5}O_2$ is better compared to that of PEG-coated CeO_2. To explain this behavior, the possible reaction between the nanoparticles and hydroxyl radicals is shown in eq 5.

$$Ce^{3+} + OH^{\bullet} \rightarrow Ce^{4+} + OH^{-} \qquad (5)$$

It can be seen that the Ce^{3+} oxidation state participates in the dissociation/scavenging of hydroxyl radicals. The concentration of oxygen vacancies or defects in PEG-coated $Ce_{0.5}Zr_{0.5}O_2$ has been found to be higher (A_{D1}/A_{F2g} = 1.3, OSC = 0.13), as confirmed from RAMAN and OSC studies, compared to PEG-coated CeO_2 having an A_{D1}/A_{F2g} ratio of 0.3 and an OSC value of 0.04. The formation of oxygen vacancies is associated with the Ce^{3+} concentration;[82] therefore, a high value of OSC reflects more number of Ce^{3+} in the material, which leads to a high number of reaction sites (eq 5), resulting in an enhanced scavenging ability. Another observation from Figure 11 is that the scavenging of the hydroxyl radicals increases with the concentration and attains the highest value at 190 and 150 μM for PEG-coated CeO_2 and $Ce_{0.5}Zr_{0.5}O_2$, respectively. The result indicates that at lower concentrations, i.e., <190 μM for CeO_2 and <150 μM for $Ce_{0.5}Zr_{0.5}O_2$, the number of nanoparticles is insufficient to react with the generated hydroxyl radicals used in the study. The higher concentration of defects present in the PEG-coated $Ce_{0.5}Zr_{0.5}O_2$ nanoparticles justifies the requirement of a lower concentration for effective scavenging compared to that of PEG-coated CeO_2. One more test with a higher concentration of 230 μM has been performed to verify the optimal concentration for effective scavenging. Beyond this concentration, the nanoparticles start to interrupt the maximum absorbance of MV and therefore, no further concentration is tested. Once the concentration reaches the optimum value, the scavenging is found to be the best, and it starts to reduce beyond the optimum concentration of the nanoparticles. When the number of nanoparticles is exceeded, some of the Ce^{3+} start to act as a catalyst, similar to Fe^{2+}, and produce hydroxyl radicals from a series of reactions analogous to Fanton/Haber Weiss as shown in eq 6.

$$Ce^{3+} + H_2O_2 + H^{+} \rightarrow Ce^{4+} + H_2O + OH^{\bullet} \qquad (6)$$
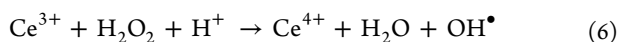
This explains the reduced scavenging by CeO_2 and $Ce_{0.5}Zr_{0.5}O_2$ nanoparticles beyond their respective optimum concentration. This hypothesis is also supported by Lu et al.,[80] where the scavenging was studied in low and high hydroxyl radical systems.

4. CONCLUSIONS

It is observed from this study that by doping zirconium into the ceria lattice and adding PEG during the synthesis stage, spherical and finer nanoparticles with a narrow size distribution are achieved. RAMAN and oxygen storage capacity studies confirmed that the smaller size of PEG-coated $Ce_{0.5}Zr_{0.5}O_2$ induced more distortion in the lattice and subsequently resulted in an increased number of oxygen vacancies, which significantly improved the scavenging activity of PEG-coated $Ce_{0.5}Zr_{0.5}O_2$ nanoparticles compared to PEG-coated CeO_2. The presence of PEG coating over the nanoparticles improved the dispersion stability of the nanofluids both in water and in PBS buffer without affecting their surface reactivity, indicating that these nanoparticles are suitable to be used in a biologically

relevant environment. From this study, it is proposed that PEG-coated $Ce_{0.5}Zr_{0.5}O_2$ with an average size of ~ 4 nm offers the best scavenging of the radicals and hence can be thought of as a potential antioxidant in a biological environment where ionic concentration of the fluid is present.

■ ASSOCIATED CONTENT

ⓈⒾ Supporting Information

The Supporting Information is available free of charge at https://pubs.acs.org/doi/10.1021/acsomega.2c01266.

> Synthesis process followed to prepare PEG-coated CeO_2 and $Ce_{0.5}Zr_{0.5}O_2$ nanoparticles (Figure S1); SEM images of the nanopartilces (a) CeO_2 (b) PEG-coated CeO_2 (c) $Ce_{0.5}Zr_{0.5}O_2$ (d) PEG-coated $Ce_{0.5}Zr_{0.5}O_2$ (Figure S2); particle size distribution histogram plot of nanoparticles (a) CeO_2 (b) PEG-coated CeO_2 (c) $Ce_{0.5}Zr_{0.5}O_2$ (d) PEG-coated $Ce_{0.5}Zr_{0.5}O_2$ (Figure S3); SEM image and elemental mapping of PEG-coated $Ce_{0.5}Zr_{0.5}O_2$. The sample was drop casted on aluminium foil wrapped glass sheet and dried in oven at 60 °C followed by placing over conducting carbon tape (Figure S4); viscosity vs shear stress of nanofluids at 37 °C (Figure S5); normalized weight loss percentage of nanoparticles in the temperature range of 300−800 °C during second heating cycle (Figure S6); reaction of hydroxyl-free radicals with methyl violet and corresponding decrease of maximum absorbance of methyl violet (Figure S7) (PDF)

■ AUTHOR INFORMATION

Corresponding Author

S. Kanagaraj − *Biomedical Devices and Biomaterials Laboratory, Department of Mechanical Engineering, Indian Institute of Technology, Guwahati, Assam 781039, India;* Phone: 0361-258-2676; Email: kanagaraj@iitg.ac.in

Author

Nandani Rai − *Biomedical Devices and Biomaterials Laboratory, Department of Mechanical Engineering, Indian Institute of Technology, Guwahati, Assam 781039, India;* ⓘ orcid.org/0000-0002-9708-4866

Complete contact information is available at:
https://pubs.acs.org/10.1021/acsomega.2c01266

Notes

The authors declare no competing financial interest.

■ REFERENCES

(1) Fang, Y.-Z.; Yang, S.; Wu, G. Free Radicals, Antioxidants, and Nutrition. *Nutrition* **2002**, *18*, 872−879.

(2) Das, M.; Patil, S.; Bhargava, N.; Kang, J. F.; Riedel, L. M.; Seal, S.; Hickman, J. J. Auto-Catalytic Ceria Nanoparticles Offer Neuroprotection to Adult Rat Spinal Cord Neurons. *Biomaterials* **2007**, *28*, 1918−1925.

(3) DeCoteau, W.; Heckman, K. L.; Estevez, A. Y.; Reed, K. J.; Costanzo, W.; Sandford, D.; Studlack, P.; Clauss, J.; Nichols, E.; Lipps, J.; Parker, M.; Hays-Erlichman, B.; Leiter, J. C.; Erlichman, J. S. Cerium Oxide Nanoparticles with Antioxidant Properties Ameliorate Strength and Prolong Life in Mouse Model of Amyotrophic Lateral Sclerosis. *Nanomedicine Nanotechnology, Biol. Med.* **2016**, *12*, 2311−2320.

(4) Heckman, K. L.; Decoteau, W.; Estevez, A.; Reed, K. J.; Costanzo, W.; Sanford, D.; Leiter, J. C.; Clauss, J.; Knapp, K.; Gomez, C.; Mullen, P.; Rathbun, E.; Prime, K.; Marini, J.; Patchefsky, J.; Patchefsky, A. S.; Hailstone, R. K.; Erlichman, J. S. Custom Cerium Oxide Nanoparticles Protect against a Free Radical Mediated Autoimmune Degenerative Disease in the Brain. *ACS Nano* **2013**, *7*, 10582−10596.

(5) Niu, J.; Azfer, A.; Rogers, L. M.; Wang, X.; Kolattukudy, P. E. Cardioprotective Effects of Cerium Oxide Nanoparticles in a Transgenic Murine Model of Cardiomyopathy. *Cardiovasc. Res.* **2007**, *73*, 549−559.

(6) Chen, J.; Patil, S.; Seal, S.; McGinnis, J. F. Rare Earth Nanoparticles Prevent Retinal Degeneration Induced by Intracellular Peroxides. *Nat. Nanotechnol.* **2006**, *1*, 142−150.

(7) Colon, J.; Hsieh, N.; Ferguson, A.; Kupelian, P.; Seal, S.; Jenkins, D. W.; Baker, C. H. Cerium Oxide Nanoparticles Protect Gastrointestinal Epithelium from Radiation-Induced Damage by Reduction of Reactive Oxygen Species and Upregulation of Superoxide Dismutase 2. *Nanomedicine Nanotechnology, Biol. Med.* **2010**, *6*, 698−705.

(8) Colon, J.; Herrera, L.; Smith, J.; Patil, S.; Komanski, C.; Kupelian, P.; Seal, S.; Jenkins, D. W.; Baker, C. H. Protection from Radiation-Induced Pneumonitis Using Cerium Oxide Nanoparticles. *Nanomedicine Nanotechnology, Biol. Med.* **2009**, *5*, 225−231.

(9) Zholobak, N. M.; Sherbakov, O. B.; Babenko, L. P.; Bogorad-Kobelska, O. S.; Bubnov, R. V.; Spivak, M.; Ivanov, V. K. The Perspectives of Biomedical Application of the Nanoceria. *EPMA J.* **2014**, *5*, 136.

(10) Cai, X.; Sezate, S. A.; Seal, S.; McGinnis, J. F. Sustained Protection against Photoreceptor Degeneration in Tubby Mice by Intravitreal Injection of Nanoceria. *Biomaterials* **2012**, *33*, 8771−8781.

(11) Rubio, L.; Annangi, B.; Vila, L.; Hernández, A.; Marcos, R. Antioxidant and Anti-Genotoxic Properties of Cerium Oxide Nanoparticles in a Pulmonary-like Cell System. *Arch. Toxicol.* **2016**, *90*, 269−278.

(12) Kong, L.; Cai, X.; Zhou, X.; Wong, L. L.; Karakoti, A. S.; Seal, S.; Mcginnis, J. F. Neurobiology of Disease Nanoceria Extend Photoreceptor Cell Lifespan in Tubby Mice by Modulation of Apoptosis / Survival Signaling Pathways. *Neurobiol. Dis.* **2011**, *42*, 514−523.

(13) Wingard, C. J.; Walters, D. M.; Cathey, B. L.; Hilderbrand, S. C.; Katwa, P.; Lin, S.; Ke, P. U. C.; Podila, R.; Rao, A.; Lust, R. M.; Brown, J. M. Mast Cells Contribute to Altered Vascular Reactivity and Ischemia-Reperfusion Injury Following Cerium Oxide Nanoparticle Instillation. *Nanotoxicology* **2011**, *5*, 531−545.

(14) Das, S.; Singh, S.; Dowding, J. M.; Oommen, S.; Kumar, A.; Sayle, T. X. T.; Saraf, S.; Patra, C. R.; Vlahakis, N. E.; Sayle, D. C.; Self, W. T.; Seal, S. The Induction of Angiogenesis by Cerium Oxide Nanoparticles through the Modulation of Oxygen in Intracellular Environments. *Biomaterials* **2012**, *33*, 7746−7755.

(15) Farias, I. A. P.; dos Santos, C. C. L.; Sampaio, F. C. Antimicrobial Activity of Cerium Oxide Nanoparticles on Opportunistic Microorganisms: A Systematic Review. *Biomed Res. Int.* **2018**, *2018*, 1−14.

(16) Kargozar, S.; Baino, F.; Hoseini, S. J.; Hamzehlou, S.; Darroudi, M.; Verdi, J.; Hasanzadeh, L.; Kim, H. W.; Mozafari, M. Biomedical Applications of Nanoceria: New Roles for an Old Player. *Nanomedicine* **2018**, *13*, 3051−3069.

(17) Shah, V.; Shah, S.; Shah, H.; Rispoli, F. J.; McDonnell, K. T.; Workeneh, S.; Karakoti, A.; Kumar, A.; Seal, S. Antibacterial Activity of Polymer Coated Cerium Oxide Nanoparticles. *PLoS One* **2012**, *7*, e47827.

(18) Bas, E.; Dinh, C. T.; Garnham, C.; Polak, M.; Van de Water, T. R. Conservation of Hearing and Protection of Hair Cells in Cochlear Implant Patients' with Residual Hearing. *Anat. Rec.* **2012**, *295*, 1909−1927.

(19) O'Leary, S. J.; Monksfield, P.; Kel, G.; Connolly, T.; Souter, M. A.; Chang, A.; Marovic, P.; O'Leary, J. S.; Richardson, R.; Eastwood, H. Relations between Cochlear Histopathology and Hearing Loss in Experimental Cochlear Implantation. *Hear. Res.* **2013**, *298*, 27−35.

(20) Eastwood, H.; Pinder, D.; James, D.; Chang, A.; Galloway, S.; Richardson, R.; O'Leary, S. Permanent and Transient Effects of Locally Delivered N-Acetyl Cysteine in a Guinea Pig Model of Cochlear Implantation. *Hear. Res.* **2010**, *259*, 24−30.

(21) Scheper, V.; Schmidtheisler, M.; Lasch, F.; Von Der Leyen, H.; Koch, A.; Schwieger, J.; Büchner, A.; Lesinski-Schiedat, A.; Lenarz, T. Randomized Placebo-Controlled Clinical Trial Investigating the Effect of Antioxidants and a Vasodilator on Overall Safety and Residual Hearing Preservation in Cochlear Implant Patients. *Trials* **2020**, *21*, 1−14.

(22) Rai, N.; Raj, R.; Kanagaraj, S. Radical Scavenging of Nanoceria in Minimizing the Oxidative Stress-Induced Loss of Residual Hearing: A Review. *J. Indian Inst. Sci.* **2019**, *99*, 529−545.

(23) Dillon, C.; Billings, M.; Hockey, K. S.; DeLaGarza, L.; Rzigalinski, B. A. Cerium Oxide Nanoparticles Protect Against MPTP-Induced Dopaminergic Neurodegeneration In A Mouse Model For Parkinson's Disease. *Nanotechnology* **2011**, *3*, 451−454.

(24) Estevez, A. Y.; Pritchard, S.; Harper, K.; Aston, J. W.; Lynch, A.; Lucky, J. J.; Ludington, J. S.; Chatani, P.; Mosenthal, W. P.; Leiter, J. C.; Andreescu, S.; Erlichman, J. S. Neuroprotective Mechanisms of Cerium Oxide Nanoparticles in a Mouse Hippocampal Brain Slice Model of Ischemia. *Free Radic. Biol. Med.* **2011**, *51*, 1155−1163.

(25) Kim, C. K.; Kim, T.; Choi, I. Y.; Soh, M.; Kim, D.; Kim, Y. J.; Jang, H.; Yang, H. S.; Kim, J. Y.; Park, H. K.; Park, S. P.; Park, S.; Yu, T.; Yoon, B. W.; Lee, S. H.; Hyeon, T. Ceria Nanoparticles That Can Protect against Ischemic Stroke. *Angew. Chem. Int. Ed.* **2012**, *51*, 11039−11043.

(26) D'Angelo, B.; Santucci, S.; Benedetti, E.; Di Loreto, S.; Phani, R.; Falone, S.; Amicarelli, F.; Ceru, M.; Cimini, A. Cerium Oxide Nanoparticles Trigger Neuronal Survival in a Human Alzheimer Disease Model By Modulating BDNF Pathway. *Curr. Nanosci.* **2009**, *5*, 167−176.

(27) Perez, J. M.; Asati, A.; Nath, S.; Kaittanis, C. Synthesis of Biocompatible Dextran-Coated Nanoceria with PH-Dependent Antioxidant Properties. *Small* **2008**, *4*, 552−556.

(28) Zhai, Y.; Zhou, K.; Xue, Y.; Qin, F.; Yang, L.; Yao, X. Synthesis of Water-Soluble Chitosan-Coated Nanoceria with Excellent Antioxidant Properties. *RSC Adv.* **2013**, *3*, 6833.

(29) Saraf, S.; Neal, C. J.; Das, S.; Barkam, S.; Mccormack, R.; Seal, S. Understanding the Adsorption Interface of Polyelectrolyte Coating on Redox Active Nanoparticles Using Soft Particle Electrokinetics and Its Biological Activity. *ACS Appl. Mater. Interfaces* **2014**, *6*, 5472−5482.

(30) Karakoti, A. S.; Kuchibhatla, S. V. N. T.; Babu, K. S.; Seal, S. Direct Synthesis of Nanoceria in Aqueous Polyhydroxyl Solutions. *J. Phys. Chem. C* **2007**, *111*, 17232−17240.

(31) Hanafy, B. I.; Cave, G. W. V.; Barnett, Y.; Pierscionek, B. Ethylene Glycol Coated Nanoceria Protects against Oxidative Stress in Human Lens Epithelium. *RSC Adv.* **2019**, *9*, 16596−16605.

(32) Perez, J.; Asati, A.; Nath, S. *Synthesis of Polymer Coated Ceria Nanoparticles for Biomedical Applications* **2012**.

(33) Dong, Q.; Yin, S.; Guo, C.; Sato, T. Aluminum-Doped Ceria-Zirconia Solid Solutions with Enhanced Thermal Stability and High Oxygen Storage Capacity. *Nanoscale Res. Lett.* **2012**, *7*, 542.

(34) Sayle, T. X. T.; Cantoni, M.; Bhatta, U. M.; Parker, S. C.; Hall, S. R.; Möbus, G.; Molinari, M.; Reid, D.; Seal, S.; Sayle, D. C. Strain and Architecture-Tuned Reactivity in Ceria Nanostructures; Enhanced Catalytic Oxidation of CO to CO 2. *Chem. Mater.* **2012**, *24*, 1811−1821.

(35) Rechniqueseddy, B. M.; Khan, A.; Lakshmanan, P.; Aouine, M.; Loridant, S.; Volta, J. C. Structural Characterization of Nanosized CeO2-SiO2, CeO2-TiO2, and CeO2-ZrO2 Catalysts by XRD, Raman, and HREM T. *J. Phys. Chem. B* **2005**, *109*, 3355−3363.

(36) Priya, N. S.; Somayaji, C.; Kanagaraj, S. Optimization of Ceria-Zirconia Solid Solution Based on OSC Measurement by Cyclic Heating Process. *Procedia Eng.* **2013**, *64*, 1235−1241.

(37) Liu, Q.; Xie, L.; Liang, J.; Ren, Y.; Wang, Y.; Zhang, L.; Yue, L.; Li, T.; Luo, Y.; Li, N.; Tang, B.; Liu, Y.; Gao, S.; Alshehri, A. A.; Shakir, I.; Agboola, P. O.; Kong, Q.; Wang, Q.; Ma, D.; Sun, X. Ambient Ammonia Synthesis via Electrochemical Reduction of Nitrate Enabled by NiCo2O4 Nanowire Array. *Small* **2022**, *18*, No. 2106961.

(38) Liang, J.; Chen, H.; Mou, T.; Zhang, L.; Lin, Y.; Yue, L.; Luo, Y.; Liu, Q.; Li, N.; Alshehri, A. A.; Shakir, I.; Agboola, P. O.; Wang, Y.; Tang, B.; Ma, D.; Sun, X. Coupling Denitrification and Ammonia Synthesis via Selective Electrochemical Reduction of Nitric Oxide over Fe 2 O 3 Nanorods. *J. Mater. Chem. A* **2022**, *10*, 6454−6462.

(39) Li, Z.; Ma, Z.; Liang, J.; Ren, Y.; Li, T.; Xu, S.; Liu, Q.; Li, N.; Tang, B.; Liu, Y.; Gao, S.; Alshehri, A. A.; Ma, D.; Luo, Y.; Wu, Q.; Sun, X. MnO2 Nanoarray with Oxygen Vacancies: An Efficient Catalyst for NO Electroreduction to NH3 at Ambient Conditions. *Mater. Today Phys.* **2022**, *22*, No. 100586.

(40) Chen, H.; Liang, J.; Li, L.; Zheng, B.; Feng, Z.; Xu, Z.; Luo, Y.; Liu, Q.; Shi, X.; Liu, Y.; Gao, S.; Asiri, A. M.; Wang, Y.; Kong, Q.; Sun, X. Ti2O3 Nanoparticles with Ti3+Sites toward Efficient NH3 Electrosynthesis under Ambient Conditions. *ACS Appl. Mater. Interfaces* **2021**, *13*, 41715−41722.

(41) Deng, Z.; Liang, J.; Liu, Q.; Ma, C.; Xie, L.; Yue, L.; Ren, Y.; Li, T.; Luo, Y.; Li, N.; Tang, B.; Ali Alshehri, A.; Shakir, I.; Agboola, P. O.; Yan, S.; Zheng, B.; Du, J.; Kong, Q.; Sun, X. High-Efficiency Ammonia Electrosynthesis on Self-Supported Co2AlO4 Nanoarray in Neutral Media by Selective Reduction of Nitrate. *Chem. Eng. J.* **2022**, *435*, No. 135104.

(42) Wang, Z.; Wu, H. H.; Li, Q.; Besenbacher, F.; Li, Y.; Zeng, X. C.; Dong, M. Reversing Interfacial Catalysis of Ambipolar WSe2 Single Crystal. *Adv. Sci.* **2020**, *7*, No. 1901382.

(43) Qin, T.; Wang, Z.; Wang, Y.; Besenbacher, F.; Otyepka, M.; Dong, M. Recent Progress in Emerging Two-Dimensional Transition Metal Carbides. *Nano-Micro Lett.* **2021**, *13*, No. 183.

(44) Soh, M.; Kang, D.; Jeong, H.; Kim, D.; Kim, D. Y.; Yang, W.; Song, C.; Baik, S.; Choi, I.; Ki, S.; Kwon, H. J.; Kim, T.; Kim, C. K.; Lee, S.; Hyeon, T. Ceria − Zirconia Nanoparticles as an Enhanced Multi-Antioxidant for Sepsis Treatment. *Angew. Chem., Int. Ed.* **2017**, *56*, 11399−11403.

(45) Hyeon, T. H.; Lee, S. H.; Soh, M.; Kim, C. K. Synthesis of Ultra - Small Ceria - Zirconia Nanoparticles and Ceria - Zirconia Nano Complex and Its Application As a Therapeutic Agent for Sepsis. U.S. Patent US15/145,8232017.

(46) Tsai, Y. Y.; Oca-Cossio, J.; Lin, S. M.; Woan, K.; Yu, P. C.; Sigmund, W. Reactive Oxygen Species Scavenging Properties of ZrO2-CeO2 Solid Solution Nanoparticles. *Nanomedicine* **2008**, *3*, 637−645.

(47) Xue, Y.; Zhai, Y.; Zhou, K.; Wang, L.; Tan, H.; Luan, Q.; Yao, X. The Vital Role of Buffer Anions in the Antioxidant Activity of CeO2 Nanoparticles. *Chem. Eur. J.* **2012**, *18*, 11115−11122.

(48) Singh, S.; Dosani, T.; Karakoti, A. S.; Kumar, A.; Seal, S.; Self, W. T. A Phosphate-Dependent Shift in Redox State of Cerium Oxide Nanoparticles and Its Effects on Catalytic Properties. *Biomaterials* **2011**, *32*, 6745−6753.

(49) Bhargava, K.; Arya, A.; Gangwar, A.; Singh, S.; Roy, M.; Das, M.; Sethy, N. Cerium Oxide Nanoparticles Promote Neurogenesis and Abrogate Hypoxia-Induced Memory Impairment through AMPK−PKC−CBP Signaling Cascade. *Int. J. Nanomedicine* **2016**, 1159.

(50) Wallick, D. Polyethylene Glycol. In *Handbook of Pharmaceutical Excipients*; Pharmaceutical Press, 2009; Vol. *E28*, pp 546−551.

(51) Mathur, S.; Moudgil, B. M. Mechanisms of Nonionic Polymer Adsorption on Oxide Surfaces. *Min. Metall. Explor.* **1998**, *15*, 24−28.

(52) Nabiyouni, G.; Barati, A.; Saadat, M. Surface Adsorption of Polyethylene Glycol and Polyvinyl Alcohol with Variable Molecular Weights on Zinc Oxide Nanoparticles. *Iran. J. Chem. Eng.* **2011**, *8*, 20−30.

(53) Ghadimi, A.; Saidur, R.; Metselaar, H. S. C. A Review of Nanofluid Stability Properties and Characterization in Stationary Conditions. *Int. J. Heat Mass Transfer* **2011**, *54*, 4051−4068.

(54) Caputo, F.; Mameli, M.; Sienkiewicz, A.; Licoccia, S.; Stellacci, F.; Ghibelli, L.; Traversa, E. A Novel Synthetic Approach of Cerium Oxide Nanoparticles with Improved Biomedical Activity. *Sci. Rep.* **2017**, *7*, No. 4636.

(55) Ozawa, M.; Matuda, K.; Suzuki, S. Microstructure and Oxygen Release Properties of Catalytic Alumina-Supported CeO2-ZrO2 Powders. *J. Alloys Compd.* **2000**, *303−304*, 56−59.

(56) Pyrzynska, K.; Pekal, A. Analytical Methods Application of Free Radical Diphenylpicrylhydrazyl (DPPH) to Estimate the Antioxidant Capacity of Food Samples. *Anal. Methods* **2013**, *5*, 4288−4295.

(57) Shah, P. M.; Burnett, J. W. H.; Morgan, D. J.; Davies, T. E.; Taylor, S. H. Ceria−Zirconia Mixed Metal Oxides Prepared via Mechanochemical Grinding of Carbonates for the Total Oxidation of Propane and Naphthalene. *Catalysts* **2019**, *9*, No. 475.

(58) Saifi, M. A.; Seal, S.; Godugu, C. Nanoceria, the Versatile Nanoparticles: Promising Biomedical Applications. *J. Control. Release* **2021**, *338*, 164−189.

(59) Livage, J.; Henry, C.; Sanchez, C. Sol-Gel Chemistry of Transition Metal Oxides. *Prog. Solid State Chem.* **1988**, *18*, 259−341.

(60) Uekawa, N.; Ueta, M.; Wu, Y. J.; Kakegawa, K. Characterization of CeO2 Fine Particles Prepared by the Homogeneous Precipitation Method with a Mixed Solution of Ethylene Glycol and Polyethylene Glycol. *J. Mater. Res.* **2004**, *19*, 1087−1092.

(61) Kuchibhatla, S. V. N. T.; Karakoti, A. S.; Baer, D. R.; Samudrala, S.; Engelhard, M. H.; Amonette, J. E.; Thevuthasan, S.; Seal, S. Influence of Aging and Environment on Nanoparticle Chemistry: Implication to Confinement Effects in Nanoceria. *J. Phys. Chem. C* **2012**, *116*, 14108−14114.

(62) Chen, A.; Zhou, Y.; Ta, N.; Li, Y.; Shen, W. Redox Properties and Catalytic Performance of Ceria-Zirconia Nanorods. *Catal. Sci. Technol.* **2015**, *5*, 4184−4192.

(63) Deng, J.; Zhou, Y.; Cui, Y.; Lan, L.; Wang, J.; Yuan, S.; Chen, Y. The Influence of H2O2 on the Properties of CeO2-ZrO2 Mixed Oxides. *J. Mater. Sci.* **2017**, *52*, 5242−5255.

(64) Deshpande, S.; Patil, S.; Kuchibhatla, S. V.; Seal, S. Size Dependency Variation in Lattice Parameter and Valency States in Nanocrystalline Cerium Oxide. *Appl. Phys. Lett.* **2005**, *87*, No. 133113.

(65) Nyoka, M.; Choonara, Y. E.; Kumar, P.; Kondiah, P. P. D.; Pillay, V. Synthesis of Cerium Oxide Nanoparticles Using Various Methods: Implications for Biomedical Applications. *Nanomaterials* **2020**, *10*, No. 242.

(66) Djuričić, B.; Pickering, S. Nanostructured Cerium Oxide: Preparation and Properties of Weakly-Agglomerated Powders. *J. Eur. Ceram. Soc.* **1999**, *19*, 1925−1934.

(67) Smith, C. B. *Infrared Spectral Interpretation—A Systematic Approach*; Taylor & Francis, 1999; Vol. 53.

(68) McDevitt, N. T.; Baun, W. L. Infrared Absorption Study of Metal Oxides in the Low Frequency Region (700-240 Cm-1). *Spectrochim. Acta* **1964**, *20*, 799−808.

(69) Karakoti, A. S.; Singh, S.; Kumar, A.; Malinska, M.; Kuchibhatla, S. V. N. T.; Wozniak, K.; Self, W. T.; Seal, S. PEGylated

Nanoceria as Radical Scavenger with Tunable Redox Chemistry. *J. Am. Chem. Soc.* **2009**, *131*, 14144−14145.

(70) Wang, Y.; Olson, E. S. Cochlear Perfusion with a Viscous Fluid. *Hear. Res.* **2016**, *337*, 1−11.

(71) Schmitt, R.; Nenning, A.; Kraynis, O.; Korobko, R.; Frenkel, A. I.; Lubomirsky, I.; Haile, S. M.; Rupp, J. L. M. A Review of Defect Structure and Chemistry in Ceria and Its Solid Solutions. *Chem. Soc. Rev.* **2020**, *49*, 554−592.

(72) Xu, Y.; Wang, F.; Liu, X.; Liu, Y.; Luo, M.; Teng, B.; Fan, M.; Liu, X. Resolving a Decade-Long Question of Oxygen Defects in Raman Spectra of Ceria-Based Catalysts at Atomic Level. *J. Phys. Chem. C* **2019**, *123*, 18889−18894.

(73) Loridant, S. Raman Spectroscopy as a Powerful Tool to Characterize Ceria-Based Catalysts. *Catal. Today* **2021**, *373*, 98−111.

(74) Montini, T.; Melchionna, M.; Monai, M.; Fornasiero, P. Fundamentals and Catalytic Applications of CeO2-Based Materials. *Chem. Rev.* **2016**, *116*, 5987−6041.

(75) Muhich, C.; Steinfeld, A. Principles of Doping Ceria for the Solar Thermochemical Redox Splitting of H2O and CO2. *J. Mater. Chem. A* **2017**, *5*, 15578−15590.

(76) Hwang, Y.; Lee, J. K.; Lee, C. H.; Jung, Y. M.; Cheong, S. I.; Lee, C. G.; Ku, B. C.; Jang, S. P. Stability and Thermal Conductivity Characteristics of Nanofluids. *Thermochim. Acta* **2007**, *455*, 70−74.

(77) Kumar, A.; Das, S.; Munusamy, P.; Self, W.; Baer, D. R.; Sayle, D. C.; Seal, S. Behavior of Nanoceria in Biologically-Relevant Environments. *Environ. Sci. Nano* **2014**, *1*, 516−532.

(78) Matter, F.; Luna, A. L.; Niederberger, M. From Colloidal Dispersions to Aerogels: How to Master Nanoparticle Gelation Nano Today From Colloidal Dispersions to Aerogels: How to Master Nanoparticle Gelation. *Nano Today* **2020**, *30*, No. 100827.

(79) Celardo, I.; Pedersen, J. Z.; Traversa, E.; Ghibelli, L. Pharmacological Potential of Cerium Oxide Nanoparticles. *Nanoscale* **2011**, *3*, 1411.

(80) Lu, M.; Zhang, Y.; Wang, Y.; Jiang, M.; Yao, X. Insight into Several Factors That Affect the Conversion between Antioxidant and Oxidant Activities of Nanoceria. *ACS Appl. Mater. Interfaces* **2016**, *8*, 23580−23590.

(81) Xue, Y.; Luan, Q.; Yang, D.; Yao, X.; Zhou, K. Direct Evidence for Hydroxyl Radical Scavenging Activity of Cerium Oxide Nanoparticles. *J. Phys. Chem. C* **2011**, *115*, 4433−4438.

(82) Gupta, A.; Das, S.; Neal, C. J.; Seal, S. Controlling the Surface Chemistry of Cerium Oxide Nanoparticles for Biological Applications. *J. Mater. Chem. B* **2016**, *4*, 3195−3202.